Impact of Platinum Loading and Layer Thickness on Cathode Catalyst Degradation in PEM Fuel Cells

Journal of The Electrochemical Society, 2023 **170** 024506

Impact of Platinum Loading and Layer Thickness on Cathode Catalyst Degradation in PEM Fuel Cells

Patrick Schneider,[1,z] Mariah Batool,[2] Andres O. Godoy,[2] Rajveer Singh,[1] Dietmar Gerteisen,[1] Jasna Jankovic,[2,z,*] and Nada Zamel[1,z]

[1] *Fraunhofer Institute for Solar Energy Systems, ISE, Freiburg, Germany*
[2] *University of Connecticut UCONN, United States of America*

In this work we investigate the effect of platinum loading and layer thickness on cathode catalyst degradation by a comprehensive in situ and STEM-EDS characterization. To decouple the effect of the platinum loading and layer thickness from each other, the experiments were categorized in two sets, each with cathode loadings varying between 0.1 and 0.4 $mg_{Pt}\,cm^{-2}$: (i) Samples with a constant Pt/C ratio and thus varying layer thickness, and (ii) samples with varying Pt/C ratios, achieved by dilution with bare carbon, to maintain a constant layer thickness at different platinum loadings. Every MEA was subjected to an accelerated stress test, where the cell was operated for 45,000 cycles between 0.6 and 0.95 V. Regardless of the Pt/C ratio, a higher relative loss in electrochemically active surface area was measured for lower Pt loadings. STEM-EDS measurements showed that Pt was mainly lost close to the cathode—membrane interface by the concentration driven Pt^{2+} ion flux into the membrane. The size of this Pt-depletion zone has shown to be independent on the overall Pt loading and layer thickness, hence causing higher relative Pt loss in low thickness electrodes, as the depletion zone accounts for a larger fraction of the catalyst layer.
 [DOI: 10.1149/1945-7111/acb8df]

Manuscript submitted August 3, 2022; revised manuscript received December 20, 2022. Published February 14, 2023. *This paper is part of the JES Focus Issue on Frontiers of Chemical/Molecular Engineering in Electrochemical Energy Technologies in Honor of Robert Savinell.*

List of Symbols

C_{DL}	Double layer capacity
L	Inductivity
R_{CL}	protonic catalyst layer resistance
R_{HFR}	High frequency resistance
Z_{RC}	R/C Impedance
Z	Total Impedance Transition Line Model
ω	angular frequency

The catalyst layer (CL) of the polymer electrolyte membrane (PEM) fuel cell is often referred to as the heart of the cell, where the electrochemical reactions take place. Sandwiched between the gas diffusion layers (GDL) and the electrolyte membrane, the CL also provides pathways for the reactant and product transport. In general, four requirements must be met and considered when discussing the cathode catalyst: (1) existence of highly-dispersed Pt-sites with high catalytic activity on which the reactions occur, (2) continuous path for efficient transport of protons, (3) continuous pore network for the transport of reactants and efficient water removal, and (4) continuous passage for the conduction of electrons within the catalyst layer. To fulfill these requirements, its structure is hence heterogeneous and complex and must be optimized to increase the reaction rates and mass transport, as well as meet the necessary technical and economical requirements of the cell. Throughout the years, this optimization, especially on the cathode side, has been mainly carried out by engineering the layers design and is mainly focused on the reduction of the catalyst loading.[1] Further reduction of the Pt loading $<0.1\,mg\,cm^{-2}$ is still needed for PEM fuel cells to become competitive.[2] However, this further reduction must not come at the expense of the durability of the cell.

Conventional catalyst layers are produced using a homogeneous suspension composed of carbon supported Pt nanoparticle catalysts (Pt/C), perfluorosulfonic acid (PFSA) ionomer binder and a solvent. Each of these ingredients affect the overall morphology and structure of the catalyst layer. For instance, the choice of carbon defines the pore size distribution and the dispersion of ionomer within the catalyst layer.[3–5] The solvent properties govern the rheology of the ink and hence its dispersion either on the membrane, gas diffusion layer or a decal foil, while the Pt loading and Pt/C weight ratio affect the thickness of the layer. The influence of each of these parameters on the performance of the cell has been studied extensively in literature.[6–14] All these factors play a role in determining Pt utilization and its effectiveness, as well as the cell durability (namely carbon corrosion and Pt dissolution rates). Hence, their effect on the catalyst layer microstructure is important to consider.

Degradation of PEM fuel cells is discussed in terms of three main mechanisms; mechanical, chemical and electrochemical processes, and is often quantified in terms of voltage loss per hour of cell operation. In the CL, electrochemical degradation is the main driver for performance loss. The electrochemical active surface area (ECSA) is often used to quantify loss of electrocatalyst and is associated with dynamic operation, for instance, cathode potential varying between 0.6 and 0.95 V or rising temporarily above 1.35 V during startup and shutdown.[15] Under such potentials, Pt becomes electrochemically unstable and may be subject to dissolution. Pt^{2+} Ions dissolved into the electrolyte can diffuse through the CL and redeposit within the CL or migrate all the way into the membrane. Hence, change of Pt distribution is expected and is the main driver for this type of degradation. Several mechanisms of Pt degradation are generally considered: (i) Pt grain migration on the carbon support, (ii) Pt dissolution and the re-deposition on larger particles (Ostwald ripening), (iii) Pt dissolution and migration into the membrane and (iv) detachment of Pt particles due to carbon corrosion.[16] Due to events of jumps to high potentials, such as in startup/shutdown operation, carbon corrosion may lead to morphology and porosity changes, loss of the electrical conductivity of the CL, loss of CL thickness and loss of the supported Pt catalyst.[17]

Changes in the CL microstructure due to Pt dissolution and carbon support degradation are extensively investigated in literature. As fuel cell degradation often occurs over a long period of time and is therefore expensive to investigate experimentally, accelerated stress tests (AST) are usually performed, following the U.S. Department of Energy (DOE) protocols, to investigate material durability in a relatively short period of time.[18] Various aspects that can affect the electrochemical degradation of the catalyst layer are of

*Electrochemical Society Member.
[z]E-mail: patrick.david.schneider@ise.fraunhofer.de; jasna.jankovic@uconn.edu; nada.zamel@ise.fraunhofer.de

particular importance. These can be (i) catalyst layer properties (Pt loading, type of carbon support, Pt/C weight ratio, solvent used, catalyst layer thickness), (ii) upper potential limit (UPL) and lower potential limits (LPL) and (iii) shape of the potential sweep.

The effect of Pt loading on carbon support degradation was examined by Harzer et al.[19] Accelerated stress tests based on square and triangular waves between 0.6 and 1.0 V_{RHE} were used to investigate the degradation of the support in cathodes with loadings of 0.4 and 0.1 mg_{Pt} cm^{-2}. Square waves were found to cause a more rapid loss of ECSA and mass activity compared to triangular waves, namely due to longer hold periods at high potentials; same finding is discussed in the work of Schneider et al.[20] Oxygen transport resistance was found to be mainly dependent on the available Pt surface area with carbon corrosion having an insignificant effect on this resistance. To increase the durability and essentially the lifetime of low loaded catalyst layer, the authors suggested that the upper potential must be limited to 0.85 V_{RHE}. With this upper potential these layers were found to sustain the 30,000 potential cycles without degradation of the H_2/air performance. The effect of upper and lower potential limits, as well as the shape of the applied load profiles was also investigated in publications by Schneider and Kneer et al.[20,21] Fairweather et al.[22] investigated the impact of carbon corrosion and related ECSA and performance loss on the water balance by neutron imaging and observed increasing water retention for corroded electrodes.

Darab et al.[23] investigated the effect of the catalyst layer thickness on the degradation of the layer with the different Pt/C ratios and the same Pt loading of 0.1 mg_{Pt} cm^{-2}. The protocol followed for the accelerated stress test involved an upper potential limit of 1.5 V. Beginning of life tests showed that the performance of the cell is independent of the Pt/C ratio and is purely dependent on the Pt loading of the cell. However, voltage losses of the catalyst layer produced with 10 wt% Pt/C ratio appeared to be higher after the accelerated stress test. They suggested that this is due to a transition in the kinetics as well as migration and oxygen diffusion in the agglomerates of this sample that are otherwise not noticeable in higher Pt/C ratios. Overall, their results indicate that for all catalyst layers investigated, both carbon and Pt degradation occurred simultaneously as the particle size increased, while the ECSA, the CL thickness and the average pore size decreased. Investigating the polarization curves and impedance spectra after degradation, they found a difference in the electrochemical behavior of the catalyst layers manufactured with 10 wt% Pt/C ratio. They suggested this difference to be mainly associated with a regime that is controlled by kinetics, migration and oxygen diffusion in agglomerates that is not otherwise seen in higher catalyst surface area per volume samples. From their findings, they concluded that carbon corrosion seems to be independent of the thickness of the layer. This is in line with the findings of Hegge et al.[24] where performance loss was attributed to the Pt ECSA loss, while carbon corrosion was independent of the thickness of the layer. Their investigation was tailored to finding the origins of performance loss due to carbon support corrosion. They concluded that the majority (~79%) of the performance degradation was caused by mass transport resistances (MTR), while the remaining losses were associated with kinetic and ohmic overpotential. The cause of the increased MTR was mainly attributed to structural changes in the catalyst layer, which were analyzed via focused ion beam scanning electrode microscope (FIB-SEM) tomography and limiting current density measurements. They concluded that the structural changes to the pore space of the CL is not the main contributor for the observed performance loss as the calculated pore space MTR was small in comparison to the total MTR. Their electrochemical and structural changes analysis showed that the increase in the resistance was mainly attributed to a loss in the active surface area and an increased water uptake with a small proportion of this increase attributed to other resistances, such as the MPL/CL interface change. Schuler et al.[25] investigated the MTR in the CL with hydrogen limiting current measurements for different Pt loadings and I/C ratios. They evaluated the CL sub-resistances by continuum multiscale modeling and found that the majority of the layers resistance can be accounted to the interfacial resistance and local transport resistance at the Pt site.

Kneer et al.[26] investigated the effect of voltage cycling on the performance of automotive membrane electrode assemblies and their electrodes' microstructure. They observed that the ECSA loss is very much dependent on the shape of the voltage cycle used (square versus triangular waves) as well as their respective lower potentials. Although the lower potential was varied, the upper potential limit was kept constant at 0.9 V to avoid carbon corrosion. Postmortem analysis was used to evaluate the structural changes of the electrode. Scanning electron microscopy (SEM) analysis of the thickness and porosity of the electrode confirmed that negligible changes to these two parameters have occurred; hence, eliminating carbon corrosion as a source of ECSA loss. While on the other hand, transmission electron microscopy (TEM) analysis revealed Pt redistribution through Pt particle growth, Pt band in the membrane and Pt depletion at the electrode/membrane interface, as the source of the ECSA loss measured. 92% of the Pt mass was found to still be present in the electrode, implying that Pt particle growth is the main source of ECSA loss in catalyst degradation. They suggested that as long as Pt dissolution and Pt particle growth are the main degradation mechanism, the performance of the membrane electrode assembly (MEA) can be predicted simply by measuring or modeling the ECSA over the lifetime of the MEA. Based on understanding such fundamentals of the degradation mechanism in the catalyst layer, efforts have also been tailored to predicting the state of health (SOH) and remaining useful life (RUL) of the fuel cell dependent on its history. These studies are always based on electrochemical indicators, such as the ECSA loss, voltage loss and changes in the impedance spectra. The reader is referred to various works in the literature, which cover this topic.[27–32,36]

Meyer et al.[32] suggested the use of electrochemical impedance spectroscopy as a monitoring tool for the evolution of carbon corrosion. They investigated the low frequency arc up to 0.01 Hz and its evolution during accelerated stress tests. The initial reduction of the inductive arc, up to 150 cycles, was associated with decreased oxygen transport resistance, attributed to the increased porosity of the carbon nanoparticles. Between 150–600 cycles, the interfacial resistance starts to play a part in the oxygen transport resistance. They argued this based on an evolution of the spectrum showing a decrease in capacitance and an increase inductance and resistance. They argued that such methods can be used to monitor individual cells to ensure they are replaced prior to complete failure of the stack.

The literature overview above highlights that the most significant indicator of catalyst degradation is the loss of catalyst active area. This becomes more important once the Pt loading is reduced to the needed values below 0.1 mg_{Pt} cm^{-2} to achieve commercialization. At such loadings, transport resistances related to the ionomer film surrounding the catalyst sites must also be explored and understood.[14,33–36] Weber and Kusoglu argued that the interactions between film and catalyst site must be understood to develop tools, structures and materials to achieve the optimum ingredients and better catalyst utilization, and hence improved catalyst layer performance.[33] Owejan et al.[14] investigated the effect of layer structuring on low loaded catalyst layers. In this context, they investigated the impact of Pt dispersion on the local oxygen transport resistances near the Pt surface by diluting various wt% Pt on Vulcan catalysts with bare Vulcan. With such an experimental campaign they were able to attribute transport resistance not only to the actual Pt surface area, but also to the surface area of the ionomer that covers the Pt and the carbon that surrounds it. Transport resistance through the ionomer film is hence a function of both Pt surface area and Pt particle dispersion. Therefore, the reduction of oxygen transport flux through the gas/ionomer interface to the Pt surface is required for the reduction of the transport loss and can be achieved

by electrode design. Again, Orfanidi et al.[34] concluded that not only ionomer film thickness, but also its distribution is the key to high performing low Pt loaded electrodes.

In this work, we combine the various insights gained so far about catalyst layer degradation in general and apply this knowledge to improve the understanding of Pt catalyst degradation. Specifically, we focus on investigating the effect of Pt loading and catalyst layer thickness on the degradation mechanism. The DOE ageing protocol is used for the durability testing and the catalyst layer is fully characterized during aging. Post-mortem analysis through SEM, scanning/transmission electron microscopy (S/TEM) and energy dispersive X-ray spectroscopy (EDS) was used to investigate the structural changes in the catalyst layers after catalyst degradation.

Experimental

Production of catalyst coated membranes.—In this study we investigate the impact of Pt loading and layer thickness on the cathode catalyst degradation by voltage cycling. For this objective, we produced a total of 7 MEAs with varying cathode loadings, CL thicknesses, and Pt/C weight ratios—which were achieved by dilution with bare carbon. Table I gives an overview of the samples considered in this study.

The first test batch (un-diluted CLs) considers MEAs with varying Pt loadings between 0.10 and 0.41 $mg_{Pt}\,cm^{-2}$ and a constant Pt/C ratio of 40 wt%. For this batch, the layer thickness scales linearly with the platinum loading.[6] To decouple the CLs Pt loading and thickness from each other, in a second batch, the layer thickness was kept constant, while Pt loading was varied by changing Pt/C ratio by diluting the same 40 wt% Pt/C catalyst powder with bare carbon (diluted CLs). Similar dilution procedures to maintain a constant layer thickness were already carried out by other groups.[14,25]

The catalyst layers investigated in this study have all been produced in-house via screen-printing on a decal substrate. We used a homogeneous suspension composed of 40 wt% platinum on carbon (Vulcan), Aquivion® (D79–25BS, liquid dispersion, 25% in water, PFSA eq. wt. 790 g mol^{-1} SO_3H, stabilized CF_3 polymer chain ends, Sigma-Aldrich Chemie GmbH, Schnelldorf, Germany) and a mixture of organic solvents (50 Vol% ethylene glycol, 50 Vol% propylene glycol methyl ether), where the suspension was homogenized by stirring. All catalyst layers were produced with a constant ionomer to carbon (I/C) ratio of 0.71. The varying Pt/C weight ratios were obtained by diluting the 40 wt% Pt/C ink with pure untreated carbon black (Vulcan XC 72 R, Fuel Cell Store) using a magnetic stirrer. All catalyst layers were transferred onto a Nafion membrane containing an anode catalyst layer with a Pt loading of 0.05 mg cm^{-2}. The cathode catalyst layer transfer was carried out at a compression of 5 MPa (referred to the printed catalyst area of 20 cm^2) and 180 °C for 15 min, producing catalyst coated membranes (CCM) with an active area of 12 cm^2. A H23C9 GDL from Freudenberg was used as a gas diffusion layer on both the cathode and anode sides.

In-Situ characterization and catalyst degradation protocol.—Every MEA stated in Table I was subjected to a comprehensive in situ characterization including an AST focusing on catalyst degradation. The AST was adapted from a protocol proposed by the DOE, where the cell is operated for 45,000 cycles between 0.6 and 0.95 V, with 3 s dwell time at each potential, in H_2 / N_2 atmosphere, at 80 °C and 100% relative gas humidity at anode and cathode. A comprehensive in situ characterization was carried out at begin of test (BoT), end of test (EoT), as well as at various time steps in-between. The tests were carried out on an in-house developed test bench using a Baltic ISE qCf Liquid Cooling high amp zero gradient test cell with a 12 cm^2 active area. The cells were compressed with 1.35 MPa clamping pressure. The following methods were applied during testing:

- Polarization curves: The cell current was measured at distinctive points between open circuit voltage (OCV) and 0.2 V, at H_2 / air (with 2 and 5 NLPM respectively), 80 °C, 2 bara gas pressure and 100% relative gas humidity. Each point was averaged over 30 s, after conditioning for a minimum of 5 min, and until a stability of $< 1\%$ was reached.
- Cyclic Voltammetry (CV): The cell was cycled 5 times between 0.05 and 0.6 V with 1 NLPM H_2 on the anode and no flow on the cathode. The measurements were carried out at 80 °C and 100% relative gas humidity. The ECSA was averaged from the H_2 adsorption and desorption peak.
- Electrochemical impedance spectroscopy (EIS): Impedance spectra were measured at 100 mA cm^{-2} at 2 NLPM H_2 and 5 NLPM air, at 80 °C, 2 bara gas pressure and 100% relative humidity. A transition line model adapted from Makharia et al.[37] was used to analyze the spectra, which accounts for double layer capacity C_{DL}, protonic catalyst layer resistance R_{CL}, high frequency resistance R_{HFR}, charge transfer resistance R_{CT} and hardware inductivity L. The model is described by Eqs. 1 and 2:

$$Z(\omega) = \sqrt{R_{CL}\,Z_{RC}}\,\coth\left(\sqrt{\frac{R_{CL}}{Z_{RC}}}\right) + R_{HFR} + j\omega L \qquad [1]$$

$$Z_{RC} = \frac{R_{CT}}{1 + R_{CT}(j\omega)^{\varphi}C_{DL}} \qquad [2]$$

- Limiting current measurements: To further investigate the impact on the oxygen diffusion resistance, limiting current measurements were carried out according to Beuscher et al.[38,39] at 80 °C and 100% relative gas humidity. A total of 16 limiting current values were extracted from a voltage sweep from 0.60 to 0.15 V, at diluted oxygen concentrations of 1, 1.5, 2 and 2.5%, and gas pressures of 1.5, 2.0, 2.5 and 3.0 bara. The total resistance was averaged from all concentrations in each pressure level and divided into a pressure dependent (molecular diffusion) and independent part (Knudsen diffusion).

Table I. Investigated cathode catalyst layers and their properties; categorized in un-diluted samples with a constant Pt/C ratio with varying layer thickness and diluted samples with varying Pt/C ratio and constant layer thickness.

Cell	Pt loading (mg cm^{-2})	Thickness (μm)	Pt/C (wt%)
	Un-diluted catalyst layers: Constant Pt/C-ratio and increasing thickness		
1	0.10	4.09 +/− 0.38	40.0
2	0.20	8.51 +/− 1.43	40.0
3	0.32	13.01 +/− 1.73	40.0
4	0.41	15.34 +/− 0.98	40.0
	Diluted catalyst layers: Varying Pt/C-ratio and constant layer thickness		
5	0.09	16.23 +/− 2.00	14.3
6	0.20	17.25 +/− 2.29	25.0
7	0.30	15.93 +/− 0.85	33.3

Prior to the initial characterization and the AST cycling, each cell was conditioned by a Break-In procedure at 80°C and 100% relative humidity, operating for 1 h at 1.5 A cm^{-2} before cycling for 4 hours between open circuit voltage (OCV) (10 s), 0.6 V (60 s) and 0.4 V (60 s).

SEM and STEM-EDS characterization.—The microstructure and elemental distribution of BoT and EoT MEAs was characterized by SEM and TEM, as well as by the STEM-EDS at the University of Connecticut. SEM cross-sectional samples were prepared by embedding of the MEA pieces in EpoThin epoxy resin (BUEHLER, USA), polishing (Struers LaboPro-5, Denmark) and gold coating (Denton vacuum LLC, USA). SEM imaging was performed on a Teneo LV Scanning Electron Microscope (SEM, Thermo Fisher Scientific, USA) in a backscattered mode. The cathode thickness was measured from 5 different areas at 5000x magnification, taking at least 10 different line measurements, using Fiji Image J software. Samples for S/TEM-EDS were prepared by embedding a small MEA piece in a 1:1 mixture of trimethylolpropane triglycidyl ether resin (Sigma-Aldrich, USA) and 4,4′-Methylenebis (2-methylcyclohexylamine, Sigma-Aldrich, USA) hardener, followed by polymerization overnight at 60 °C, and sectioning of approximately 100 nm thin sections by Leica UCT ultramicrotome (Germany), that were placed onto 200 mesh Cu/Pd TEM grids. S/TEM imaging and EDS mapping was performed on a Talos F200X microscope (STEM, Thermo Fisher Scientific, USA), using 200 kV electron accelerating voltage. Pt particle size was determined by bright-field imaging of at least 200 particles in the cathode at 190kx magnification in at least 4 different areas by the bright field detector (BF-TEM). Particle size distribution was obtained by Fiji ImageJ. Elemental distribution mapping was performed using the same instrument by STEM-EDS, at 5kx and 79kx magnifications, with a 1000 µs dwell time for 1 cycle and electron dose of 2.34×10^4 e^-/nm^2. Pt concentration of the BoT and EoT layers was quantified from the STEM-EDS maps using ESPIRIT 1.9 (Bruker, USA) analytical software, followed by an in-house proprietary data quantification method.[26]

Results and Discussion

The following section will focus on the impact of the cathode loading and its corresponding thickness on the BoT catalyst properties, and how they evolve during the applied catalyst degradation protocol. To allow these two parameters to be considered separately from each other, the results will always be presented in two groups: Un-diluted catalyst layers with varying Pt loadings and constant Pt/C ratio, leading to proportionally increasing layer thickness (Table I, cells 1–4), and carbon diluted catalyst layers with varying Pt loadings and adjusted Pt/C ratios, leading to a constant layer thickness (Table I, cells 5–7). All parameter values discussed will be summarized again Table A·I in the appendix.

ECSA loss.—Figure 1a shows the ECSA evolution over time for all catalyst layers considered in this study. By observing the beginning of test values, an expected linear trend can be noted between the Pt loading and the achieved ECSA, for both diluted and un-diluted layers, which indicates that similar amounts of available Pt were accessible during the CV measurement. Deviations in the range of $< 5\%$ are mainly attributed to the accuracy in determining the exact layer loading by weighing.

Looking at the evolution over time, it can be noted that all investigated MEAs lose between 55 and 75% of their initial ECSA during voltage cycling. Figure 1b shows the relative losses after 45,000 cycles for each material and sets out a dependency on the catalyst loading, with a trend of higher relative ECSA loss for lower Pt loadings, and slightly higher ECSA loss for diluted samples compared to un-diluted ones. To further discuss the origin of this correlation, Fig. 2 shows STEM EDX measurements for all cathode layers, mapping out the Pt (red) and Ionomer/fluorine (green) content at the beginning and the end of test.

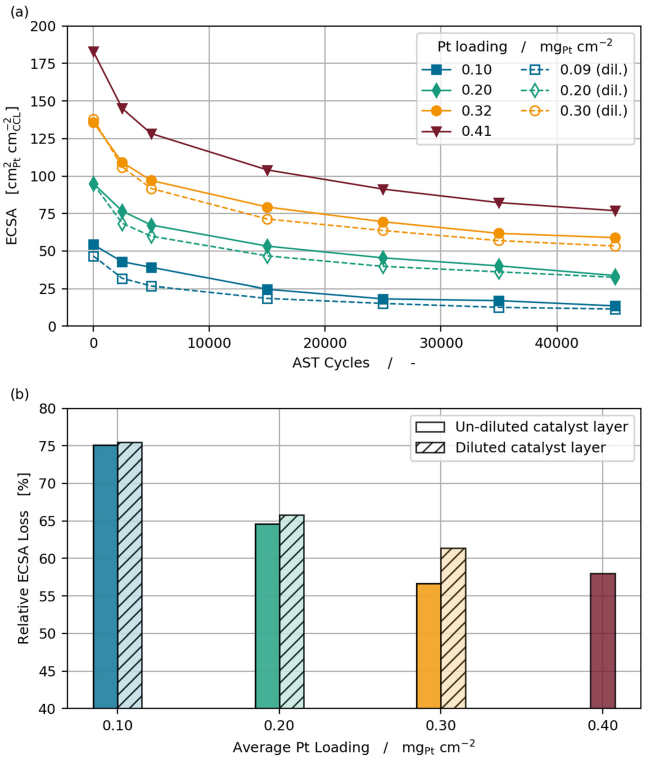

Figure 1. (a) ECSA evolution over 45000 AST cycles and (b) relative ECSA loss at EoT for diluted and un-diluted catalyst layers with varying Pt loading.

For the un-diluted layers, the BoT images show a uniform Pt distribution with a layer thickness increasing with Pt loading. One of the main driving factors behind catalyst degradation is Ostwald ripening, where Pt preferably dissolves from small particles at high potentials and redeposits at larger particles at low potentials. Instead of redepositing, Pt^{2+} ions can also diffuse through the catalyst layer into the membrane, forming a so-called Pt band. Looking at the end of test cross-sections in Fig. 2, one can see the formation of the Pt band roughly 0.5 μm away from the membrane/cathode interface.

This diffusion process can be described by Fick's law and is driven by a concentration gradient of Pt^{2+} ions Δc_{Pt2+}, and diffusion lengths L_x. The Pt^{2+} flux in the catalyst layer can be described with the diffusion coefficient of Pt^{2+} in ionomer $D_{Pt2+/Io.}$ as follows[20]:

$$q_{Pt} = D_{Pt2+/Io.} \frac{\Delta c_{Pt2+}}{L_x} \qquad [3]$$

As the uniform Pt distribution in the BoT state of the electrode causes an evenly distributed through-plane Pt dissolution and Pt^{2+} concentration during voltage cycling in H_2/N_2 atmosphere, the ion diffusion remains mainly dependent on the diffusion length or distance to the membrane interface. This effect leads to a stronger Pt loss at the membrane interface, creating a so-called Pt depletion zone with lower amounts of remaining Pt compared to the rest of the catalyst layer. At the GDL interface however, the pull towards the membrane is much smaller, causing mainly a local re-deposition of dissolved ions.

What can be noted from the cross-sections is that the size of this depletion zone seems to be independent of the total catalyst layer loading and thickness, as mainly Pt close to the membrane is lost. The effect of this Pt loss from the depletion zone on overall Pt loading for BoT and EoT samples was quantified using the STEM-EDS signal (Fig. 3). It should be noted that all quantified Pt loadings are subject to an error of 5%. The data shows that thin electrodes (low loaded, un-diluted samples) have a high Pt loss ($\sim$ 30%)

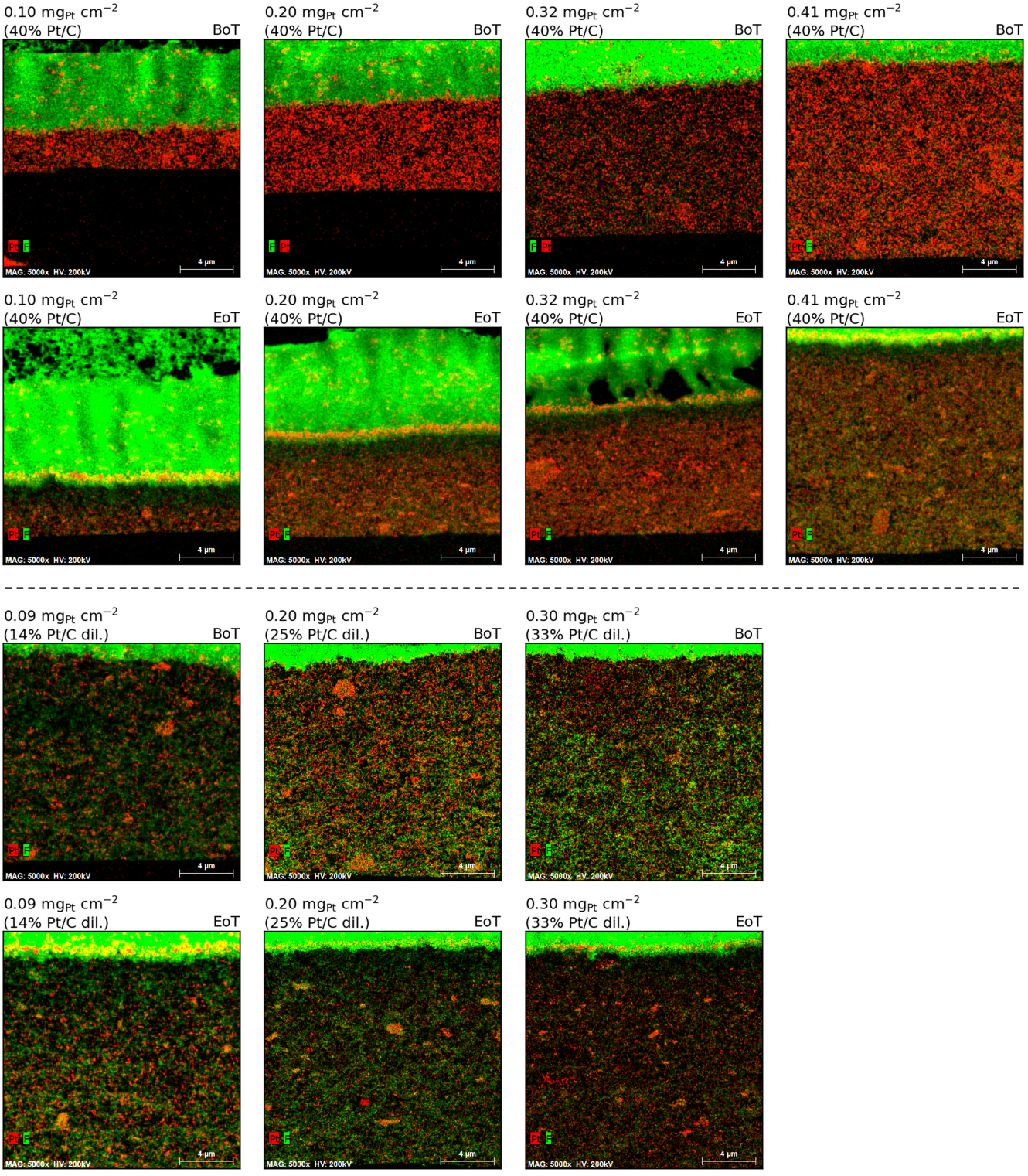

Figure 2. STEM-EDS maps showing the through plane distribution of Pt (red) and Fluoride (green); cross-sections of diluted and un-diluted cathode catalyst layers with varying Pt loading at BoT and EoT.

relative to their BoT loading, while the loss decreases with increasing thickness leading to a low relative Pt loss (∼10%) for the largest CL thicknesses. The same relative Pt loss of 10% was observed for all diluted layers with the same forced high thickness. As observed earlier, the size of the Pt depletion zone has shown to be independent on the overall CL thickness, causing a higher relative Pt loading loss for thin electrodes as the size of the Pt-depletion zone to the whole CL thickness is relatively larger. Thicker electrodes hence result in lower relative Pt loading losses, as the Pt depletion zone accounts for a smaller fraction of the overall CL. These observations are in line with the ECSA losses discussed earlier and would explain the measured increasing relative ECSA loss for lower thicknesses.

To further investigate this observation, the Pt concentration in mg_{Pt} cm^{-3} is quantified and presented in Fig. 4. Pt concentration in the whole layer and in the Pt-depleted zone (at the CL-membrane interface) was quantified for BoT and EoT samples. The observation

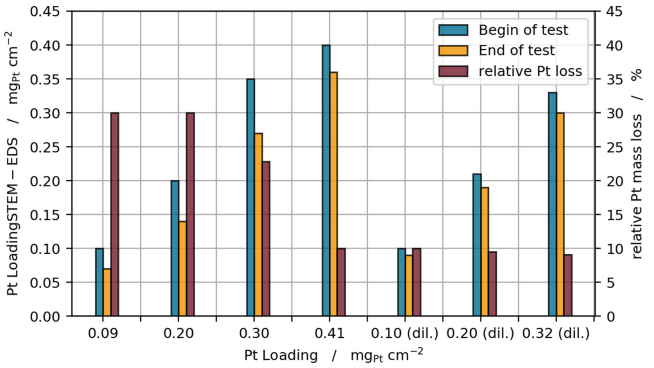

Figure 3. Quantified Pt loadings for the whole catalyst layers at BoT (blue) and EoT (orange) determined by STEM-EDS imaging, relative Pt loading loss shown as a fraction from the BoT (red).

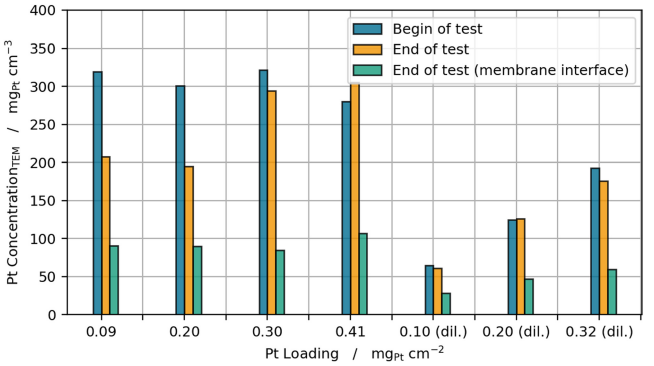

Figure 4. STEM-EDS quantified Pt concentrations for the whole catalyst layers at BoT and EoT, and in the depletion zone at EoT.

in Fig. 4 shows that the quantified BoT concentrations of the whole layer for the diluted samples increase linearly with lower degree of dilution, as intended to obtain a constant layer thickness, while the un-diluted samples show comparable Pt concentrations due to their constant Pt/C ratio. The EoT concentrations in the whole layer show almost no change for all layers with higher thickness, as the Pt-depleted zone takes up a smaller fraction of the overall layer. Only the un-diluted layers with loadings below 0.20 mg$_{Pt}$ cm^{-2} show a notable change in concentration, due to their lower thickness. For the Pt-depleted zone at the membrane interface, the quantified Pt concentration agree with the visual observations: Pt concentration in this zone is shown to be much lower than that of the rest of the layer, implying again that the total mass loss of Pt occurs mainly at the CL-membrane interface.

With this observation we propose a relative dependency of the catalyst layer thickness on the Pt mass loss into the membrane—with thinner layers leading to a higher relative Pt loss. This however leaves the question why a forced increase in thickness, as it was realized by diluting the catalyst layers ink, does not result in a decrease in ECSA loss, as the results in Fig. 1 have shown. We believe that this originates from the nature of how the catalyst powder was diluted with bare carbon. Figure 5 shows the STEM-EDS maps for all diluted samples at BoT and Eot, from which the Pt concentrations in Fig. 4 were quantified. As the Pt dissolution and re-deposition rates can be described by the Butler Volmer equation,[40] the main driving factors behind the Pt dissolution are the applied potential and the dissolved concentration of Pt^{2+} ions. The increasing Pt^{2+} concentration leads to a saturating effect after a certain time at high potentials, where the Pt^{2+} concentration in the ionomer increases locally, while the dissolution rate diminishes. However, by diluting the electrode, this saturation effect could set in much later, as every Pt particle has access to a larger reservoir of

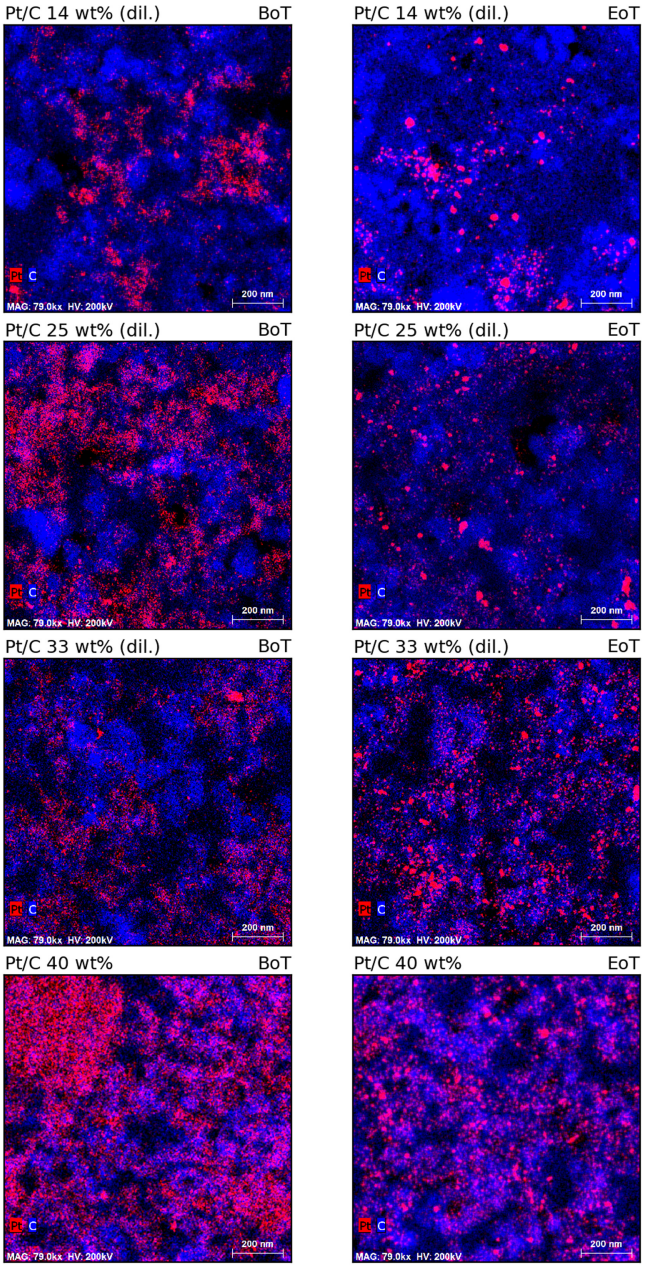

Figure 5. STEM-EDX maps of Pt (red) on carbon (blue) distribution for catalyst layers with varying degree of dilution at beginning and end of test.

ionomer to dissolve into, leading to higher dissolution rates per particle. This again would lead to a higher ECSA loss, caused by either stronger Ostwald ripening or Pt particle loss, which would hence overlap with the effect of decreasing Pt loss with higher thicknesses. As the degree of dilution increases with lower Pt loadings, this effect should become more pronounced, leading to even higher dissolution rates and ECSA losses.

In addition to mass loss caused by Pt ion flux towards the membrane, surface loss related to Ostwald ripening must be considered during Pt degradation. Figure 6 shows the BoT and EoT particle size distributions extracted from TEM images at the investigated loadings, where the change in mean particle size and standard deviation can be taken as a measure for degradation by Ostwald ripening.

While the BoT distributions show reproducible mean particle sizes of $\sim$ 2–2.5 nm for the un-diluted CL's, the EoT distributions state an increase up to 8 nm particle size. Additionally, a shallow but monotonic trend can be identified, showing a slightly higher increase

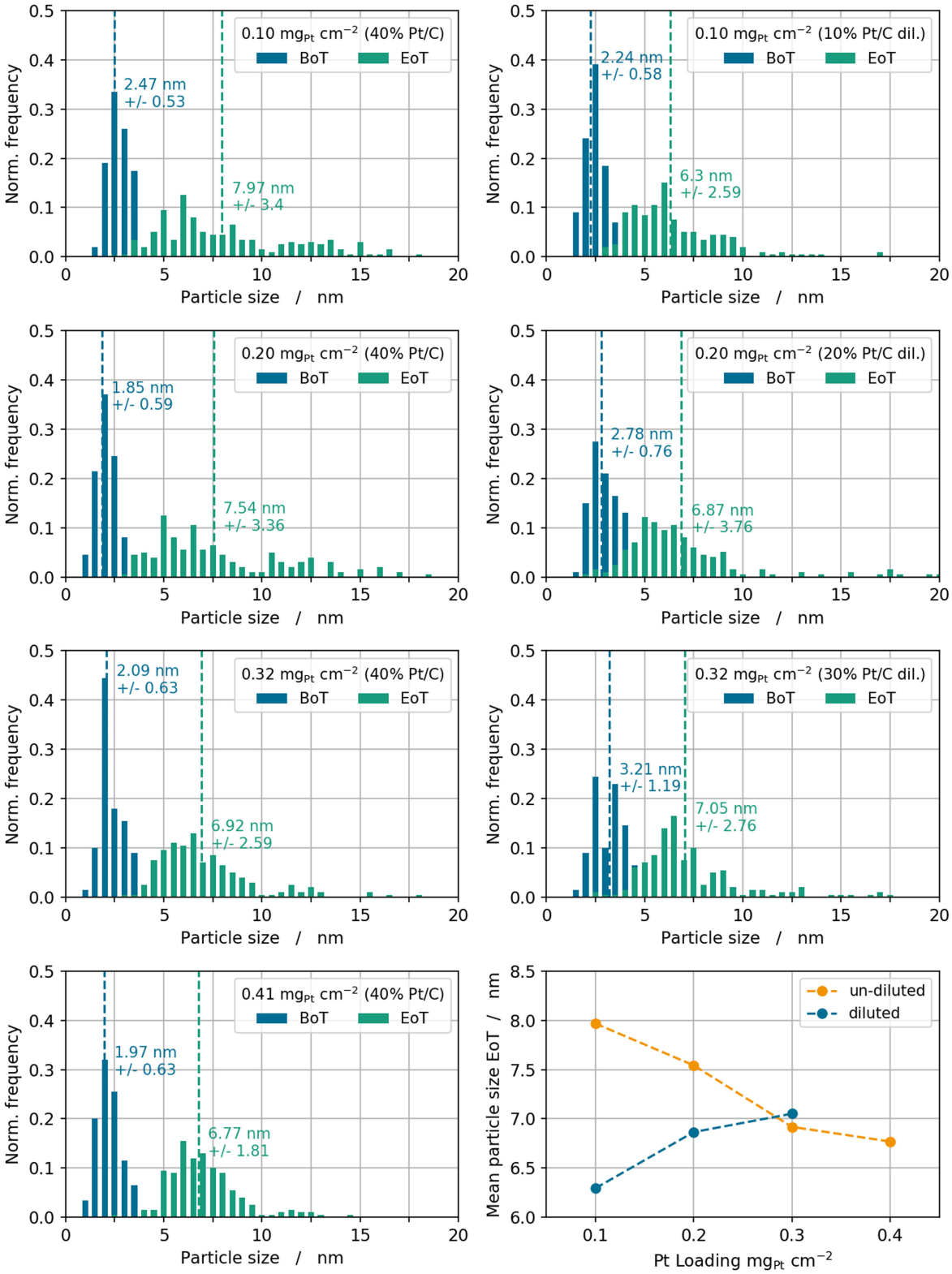

Figure 6. Pt Particle size distributions BoT and EoT of all investigated catalyst layers with varying Pt loadings and degrees of dilution. Bottom right shows summarized EoT mean particle size in relation to Pt loading.

in mean particle size and standard deviation for lower loadings, which both indicate stronger degradation due to Ostwald ripening. This would additionally support the trends related to the ECSA loss investigated in Fig. 1. The increasing trend in relative ECSA loss from high loaded to low loaded electrodes hence agrees with both the increasing relative Pt loading loss and Pt particle size growth.

The diluted samples however show overall a slightly lower particle growth, with a trend of lower EoT particle sizes for higher degrees of dilution. This indicates less Ostwald ripening with lower Pt concentrations. Due to the dilution less particles might be able to contribute to the local re-deposition process at larger particles, resulting in overall lower particle growth. As discussed earlier, the

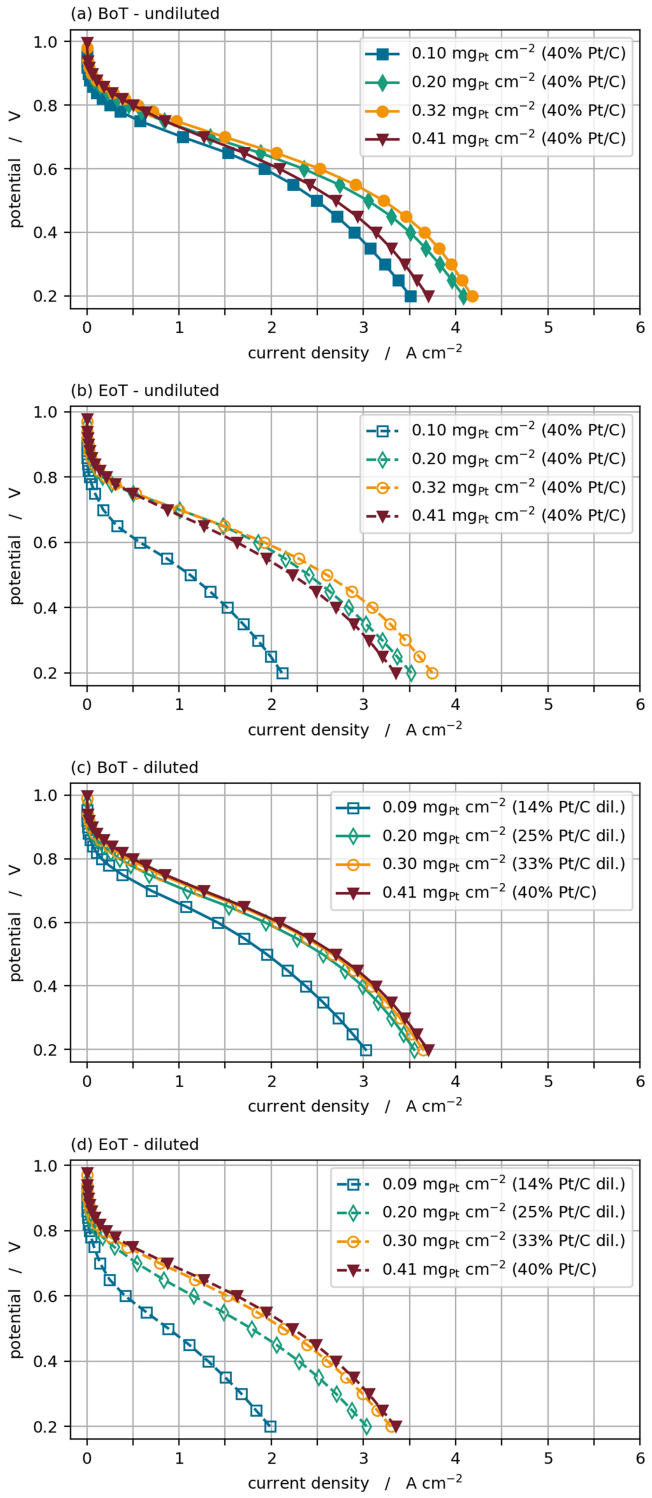

Figure 7. Performance curves measured at H_2/air, 80 °C, 2 bara pressure and 100% relative humidity: begin of test and end of test curves for diluted (unfilled markers) and un-diluted (filled markers) catalysts layers.

access to larger ionomer reservoirs might also result in higher Pt dissolutions per particle. Due to the lower amount of locally available particles, the redeposition might be hindered, leading to increased Pt loss into the membrane, and hence higher ECSA loss for lower Pt concentrations.

Cell performance.—The effect of Pt loading and thickness on the BoT and EoT cell performance is given in Fig. 7. Figure 7a shows performance curves for varying cathode loadings and layer thickness by keeping a constant Pt/C ratio. As the curves show, the overall performance increases with increasing Pt loading up to the point of 0.33 mg$_{Pt}$ cm^{-2}, while exceeding the loading further to 0.41 mg$_{Pt}$ cm^{-2} causes a performance drop related to increasing layer thickness and corresponding transport losses. A medium loading was therefore found to be the best compromise between catalyst layer activity and thickness related losses, which is in line with other studies.[40]

Figure 7c displays BoT performance curves of catalyst layers with comparable loadings as in Fig. 7a, but with constant layer thickness by adapting the Pt/C ratio accordingly. Please note that the performance curve with 0.41 mg$_{Pt}$ cm^{-2} loading and a Pt/C ratio of 40% from Fig. 7a was shown again as a reference for comparison. In this case, the impact of layer thickness is balanced out, so that the effect of Pt loading can be investigated separately. A significant performance increase is measured by increasing the Pt loading from 0.09 mg$_{Pt}$ cm^{-2} to 0.2 mg$_{Pt}$ cm^{-2}, while only marginal improvements of the polarization curves are shown for a further increase of Pt loading. Note that, even though the performance improvement is minor, its change follows the increased Pt loading since the effect of mass transport is normalized due to the same CL thickness. Figures 7b and d show the respective end of test performance curves for the diluted and un-diluted cases. A loss in performance due to catalyst degradation is clearly seen at the EoT, with the strongest decrease for the lowest Pt loading in both cases.

To further understand the origin of the performance difference in BoT samples and losses in EoT samples, the specific activity at 700 mV normalized to the respective BoT and EoT ECSA values was calculated as shown in Fig. 8. In the un-diluted case with constant Pt/C ratio, the BoT values show a clear linear trend of increasing activity with lower layer thicknesses, caused by a reduction of either proton migration or O_2 diffusion limitations. The diluted cases show a notably smaller increase of activity with lower Pt loading, as losses related to thickness changes are suppressed. The fact that the dependency of activity on Pt loading remains to some extent despite the constant thickness underline the presence of significant through-plane transport losses. The higher Pt loading leads to larger current generation which might result in increased through-plane inhomogeneities in either oxygen concentration or protonic potential coming along with higher overpotentials. Consequently, the uneven current generation leads to a decreasing specific activity with increasing Pt loading.

Comparing the EoT values in the un-diluted case, it can be seen that the specific activity after degradation for all loadings above 0.2 mg$_{Pt}$ cm^{-2} has increased, as the ECSA decreases stronger than the current density at 700 mV. An explanation could be that Pt loss occurred partly in regions that were accessible in the CV measurements but in operation hindered in sufficient accessibility of either oxygen (in pores) or protons (in non-flooded pores). Another possibility might be that the increase of the mean Pt particle size (as seen in particle size distributions in Fig. 6) causes less Pt oxide formation,[20,40] resulting in a higher specific activity. In contrary to the other loadings, the 0.1 mg$_{Pt}$ cm^{-2} CL shows a decrease in specific activity. This might be related to the strong increase in O_2 diffusion resistance, as discussed in Fig. 9.

Catalyst properties and transport resistances.—To further understand the catalyst layers behavior due to ageing, we evaluated the double layer capacity and transport properties, namely oxygen diffusion and proton resistances, using H_2/air impedance spectra and limiting current measurements.

Figure 9a shows the protonic catalyst layer resistance extracted from H_2/air impedance at 100 mA cm^{-2}. Considering the un-diluted catalyst layers with a constant Pt/C ratio, a monotonic trend can be observed of higher resistances with increasing layer thickness (due to increased Pt loading), causing longer protonic pathways and hence increased resistance. The same trend can be observed for the diluted catalyst layers with constant thickness, although the dependency on the loading is much smaller. The fact however, that this

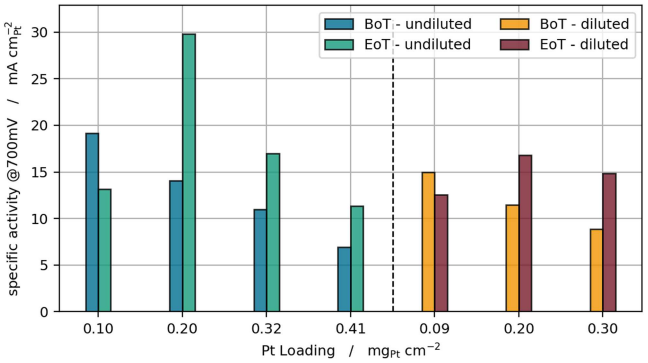

Figure 8. Specific activity at 700 mV BoT and EoT for different Pt loadings of diluted and un-diluted catalyst layers, obtained by dividing the current density at 700 mV with the respective ECSA values.

dependency is still present when the layer thickness is constant, indicates possible changes to the ionomer structure or distribution caused by the dilution. The lower Pt concentration might for instance lead to more available ionomer for the formation of protonic pathways through the layer, as less ionomer is needed to cover the available Pt. It can also be noted that the resistances for each diluted layer was measured to be slightly higher than the corresponding un-diluted case, which can be assigned to the higher layer thickness at the respective loading. Comparing the BoT and EoT values, no significant change in the resistances could be observed, which indicates that no influential ionomer re-distribution or thickness reduction occurred during testing. In case of the diluted layers it should be noted that treated carbons (as the 40 wt% Pt/C catalyst) and untreated carbons (as used for dilution) might have different interactions with the ionomer,[41] and hence could affect especially the measured protonic resistances and double layer capacity.

Figure 9b shows the pressure independent oxygen diffusion resistance, which was extracted from limiting current measurements. The pressure independent resistance accounts mainly for diffusion through small pores, the ionomer thin film and water, where molecules rather collide with the pore walls than with each other. Additionally, the pressure dependent resistance was extracted from the same measurement, which mainly accounts for larger pores in the catalyst layer, GDL and flow channels, where molecules primarily collide with each other. This resistance, however, has shown to be independent of loading and degradation state and is therefore not shown here. Looking at the BoT values of the pressure independent resistance, a trend of increasing resistances with lower Pt loadings can be observed, for both the diluted and un-diluted cases. A similar effect was already investigated by Owejan et al.,[14,42] where a lower amount of available Pt was shown to have caused higher Knudsen diffusion resistances due to a higher O_2 flux per Pt particle and hence longer diffusion lengths through the ionomer thin film. As this effect can also be seen in the diluted catalyst layers, it seems to be independent of the layer thickness and is rather related to the total amount of available Pt alone. Considering the EoT values, a strong increase in resistance can be noted for all investigated catalyst layers, which can be assigned to the overall Pt loss.

As the diffusion resistance shows a high dependency on the overall available Pt, a local diffusion resistance can be obtained by multiplying the pressure independent resistance with the respective ECSA value, providing a specific resistance at the local Pt sites. As it can be seen in Fig. 10, all observed cases show a decrease with degradation; indicating that ECSA loss partly occured in regions that are inactive at higher current densities where mass transport is limiting. This could be for instance due to Pt located deep inside pores or close to the membrane interface, where it is less accessible for oxygen. It's also notable that the EoT resistances for 0.2–0.4 mg$_{Pt}$ cm^{-2} un-diluted, as well as the BoT and EoT resistances for all diluted electrodes show very comparable values, indicating that the

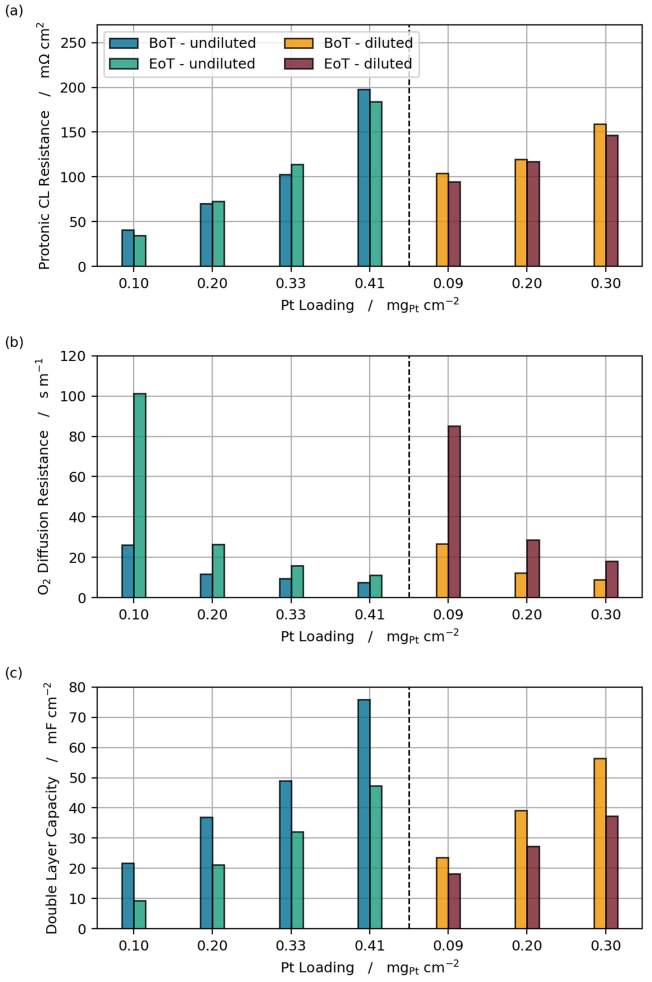

Figure 9. In-situ catalyst parameters at BoT and EoT - comparison of different Pt loadings of diluted and un-diluted catalyst layers: (a) Protonic catalyst layer resistance, (b) pressure independent O_2 diffusion resistance, (c) double layer capacity.

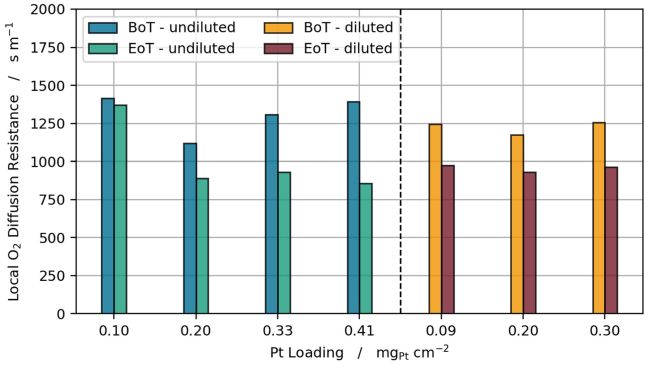

Figure 10. Local O_2 diffusion resistance at BoT and EoT, obtained by multiplying the pressure independent O_2 resistances with the respective ECSA values.

local diffusion resistance becomes independent on the Pt loading by either dilution of the electrode or degradation. The only exception is seen for the un-diluted catalyst with a 0.1 mg cm^{-2} Pt loading, which shows almost no decrease in local diffusion resistance, due to a stronger increase of the pressure independent resistance. This inconsistency of low loaded catalyst layers is however in accordance with the results reported in other publications.[13,29] A possible

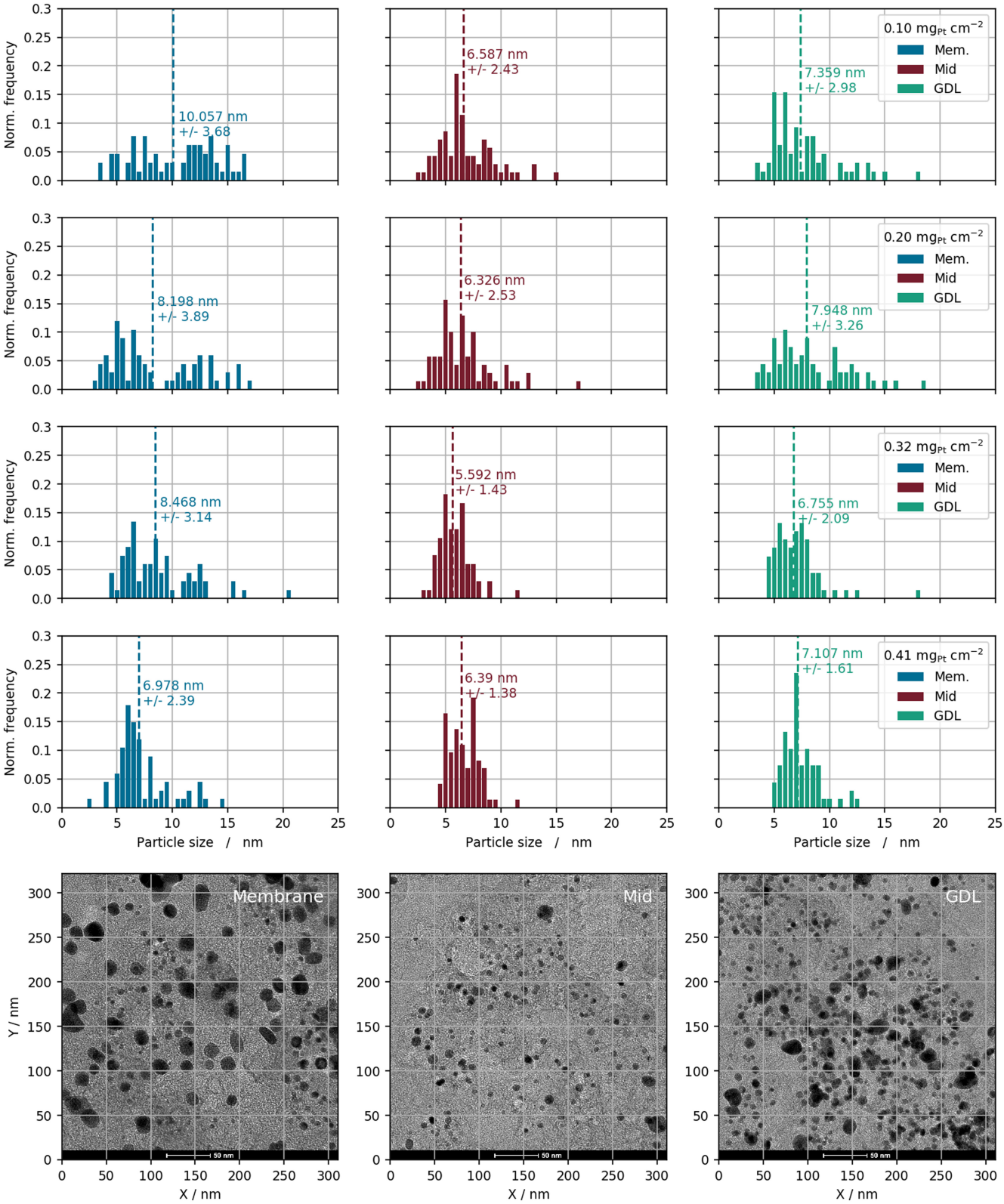

Figure 11. Pt particle size distributions after 45,000 AST cycles for catalyst layers with varying Pt loading at constant Pt/C ratio of 40%, measured independently at the membrane interface, mid-layer, and GDL interface. Exemplary TEM images shown for 0.1 mg cm^{-2} catalyst.

explanation could be the increased tendency to cell flooding due to decreasing vaporization capability of electrodes with lower thickness, as reported by Muzaffar et al.[43,44]

Figure 9c displays the double layer capacity (C_{DL}), which was again extracted from H_2/air impedance spectra at 100 mA cm^{-2}. The double layer capacity serves as a measure to describe the protonic and electric interface, which refers to the interface Pt—ionomer, Pt—water, carbon - ionomer, carbon—water. As the measurements are carried out at 100% relative gas humidity and a fixed current, we assume the amount of liquid water present to be constant. Changes in

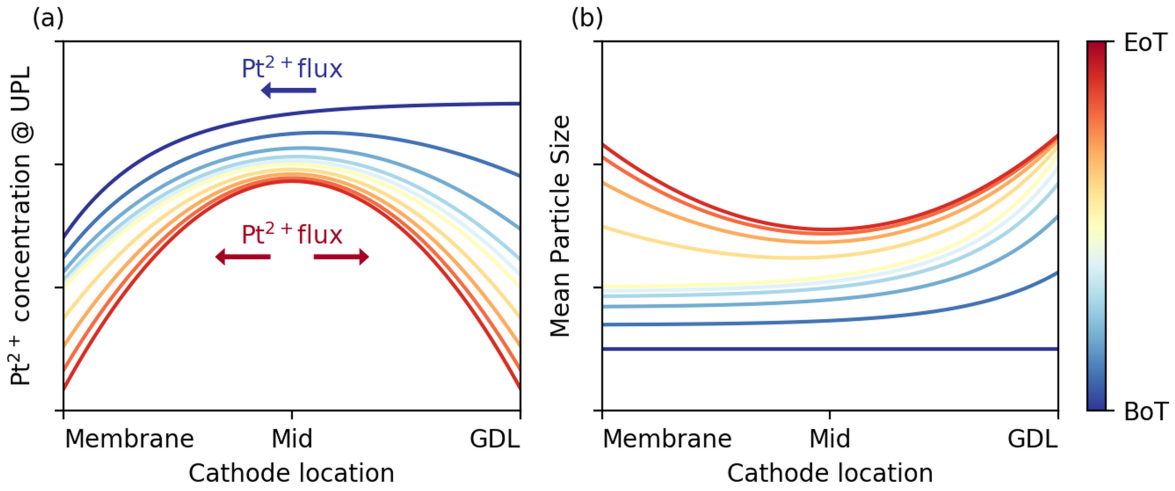

Figure 12. Qualitative description of the change in dissolved Pt2 + ion concentration at upper potential limit (a) and the resulting growth in mean particle size (b) from BoT to EoT, at the membrane interface, mid layer and GDL interface.

the BoT C_{DL} can therefore mainly be accounted to the change in interface between Pt—ionomer and carbon—ionomer. In the EoT state, however, it must be noted that a change in C_{DL} can also be attributed to a change in pore size distributions leading to a change in the interface between carbon and water. The BoT values of the un-diluted catalyst layers show a linear trend of increasing C_{DL} with increasing Pt loading, which can be mainly attributed to the linear increase in layer thickness and thus increasing interfaces. The same linear trend can be observed for the diluted catalyst layers with a forced constant thickness. The fact that the correlation to the Pt loading was measured despite the constant layer thickness supports the findings of other groups,[45,46] who state that ionomer preferably covers Pt particles rather than bare carbon surfaces. This effect was also notable in the STEM-EDS maps of the diluted samples discussed in this work. (see Fig. A·I in the appendix). Comparing the BoT and EoT values, a decrease in C_{DL} was measured for all layers. As the change in C_{DL} also accounts for the Pt—ionomer interface, this decrease might also cover the measured ECSA or Pt mass loss, which was discussed earlier in this section. Comparing the different Pt loadings, the decrease was found to be slightly lower in each respective diluted case.

Local impacts on Ostwald ripening.—In the following section we discuss the local dependency of catalyst degradation by Ostwald ripening and Pt^{2+} ion diffusion into the membrane. Figure 11 shows EoT particle size distributions at the membrane - cathode interface, mid-layer, and GDL—cathode interface for un-diluted catalyst layers with varying Pt loadings. TEM images from the catalyst layer with 0.10 mg cm^{-2} are shown in the bottom row as a representation of the Pt distribution in the aged samples. It can be noted that in all measured samples the mean particle size showed a strong increase with degradation at the membrane and GDL interface, and a significantly lower growth in the middle of the layer. Additionally, one can see that the membrane side shows mainly large particles in overall lower quantities, while the GDL side shows a mix of small to large particles in higher quantities. In the middle of the CL the number of Pt particles decreases with a moderate increase in particle size for the residual particles. To account for these local differences in particle growth, we propose a modeling approach based on a degradation model we published in an earlier work.[20] This approach comprises the Pt dissolution and redeposition in combination with a concentration driven Pt^{2+} ion flux. More comprehensive simulations on this topic are currently ongoing and will be the focus of a future publication. In this work we intend to discuss the approach in a qualitative way.

Pt particle growth or shrinkage at a certain electrode potential depends on its size-dependent equilibrium potential and the Pt^{2+} concentration in its vicinity. A higher electrode potential than the equilibrium potential leads to a Pt dissolution process which is faster for smaller particles due to their lower equilibrium potential. This dissolution process can be decelerated or even stopped if the Pt^{2+} concentration is high enough in the particle's vicinity, so that the redeposition process counterbalances the dissolution. Assuming a homogeneous particle-size distribution within the CL at BoT, a homogeneous Pt dissolution occurs within the CL at UPL during a catalyst AST, leading to an increase of the Pt^{2+} concentration in the ionomer. Since the Pt ions cannot penetrate the GDL but can diffuse into the membrane, a Pt^{2+} concentration profile will develop according to the schematic in Fig. 12a at BoT (blue line). The lower Pt^{2+} concentration at the membrane interface leads to a higher dissolution rate (especially for the small particles) than in the mid layer or close to the GDL interface. A deceleration or even a stop of the Pt dissolution kicks in first (especially for the large particles) at the GDL interface due to the highest Pt^{2+} concentration. This means for every potential cycle, the high dissolution rate at the membrane interface leads to a fast decrease (and finally total dissolution) of the small particles where with time less and less particles remain for a particle growth by redeposition at LPL. The highest redeposition rate occurs at the GDL interface due to the highest Pt^{2+} concentration, leading to a strong particle growth without losing too many particles in total. The growth process of these particles near the GDL interface leads to a reduced dissolution process and therefore to a lowered Pt^{2+} concentration at UPL. Consequently, a non-monotonic Pt^{2+} concentration profile develops leading to a Pt ion flux from the mid layer to the GDL interface (Fig. 12a at EOT (red line)). The missing Pt^{2+} ions in the mid layer provoke the lowest redeposition rate in relation to the dissolution process, leading to a moderate Ostwald ripening (Fig. 12b).

Conclusions

In this work we investigated the impact of Pt loading and layer thickness on cathode catalyst layer degradation by in situ characterization and STEM-EDS imaging. A total of 7 MEA's with varying cathode Pt loadings between 0.1 and 0.4 mg_{Pt} cm^{-2} and Pt/C weight ratios between 14 and 40 wt% were produced and tested. The experiments were categorized in two sets: (i) un-diluted samples with constant Pt/C ratio, and hence linearly increasing layer thickness, and (ii) diluted samples with varying Pt/C ratios to achieve a constant layer thickness. Every MEA was subjected to a comprehensive in situ characterization including limiting current measurements, impedance spectroscopy, polarization curves, cyclic voltammetry, and an accelerated stress test where the cell was

operated for 45,000 cycles between 0.6 and 0.95 V. All samples were additionally analyzed at beginning and end of test by SEM and STEM-EDS.

While all conducted tests showed a relative ECSA loss between 55 and 75% after aging, a trend of higher ECSA loss with lower Pt loadings was observed for both diluted and un-diluted samples. STEM-EDS measurements of the cathode cross-sections showed that Pt was mainly lost close to the membrane—cathode interface, creating a so-called depletion zone. It was also observed that the size of the depletion zone showed to be independent of the total catalyst layer loading and thickness. In low loaded catalyst layers the depletion zone hence represents a larger part of the whole electrode, leading to a higher relative Pt and ECSA loss. This implies a relative dependency of the catalyst layer thickness on the Pt mass loss into the membrane, with thinner layers leading to higher relative Pt loss. However, the diluted catalyst layers with varying Pt/C ratios have a shown similar loading dependent ECSA loss, despite their constant thickness. The increased ECSA loss with higher degree of dilution might originate from an increased Pt dissolution per Pt particle, as each Pt particle has access to a larger reservoir of ionomer to dissolve into. This causes a delayed saturation in Pt^{2+} concentration, leading to higher dissolution rates with higher degrees of dilution and hence allowing stronger ECSA loss.

Particle size analysis of the un-diluted samples showed a shallow but consistent trend of higher Pt particle growth for lower Pt loadings, indicating stronger Ostwald ripening in thinner electrodes and hence increased ECSA loss.

The performance of the un-diluted MEA's showed a strong increase in performance from 0.1 to 0.2 mg_{Pt} cm^{-2}, and only moderate improvement by further increasing the loading. A performance drop was measured when increasing the loading from 0.3 to 0.4 mg_{Pt} cm^{-2}, which has shown to be related to the increasing layer thickness and corresponding transport losses. The diluted layers, where the impact of layer thickness is balanced out by adapting the Pt/C ratio accordingly, showed monotonically increasing performances with higher loadings, with significant increase from 0.1 to 0.2 mg_{Pt} cm^{-2}, and only marginal improvements for further increase of Pt loading.

The protonic layer resistance showed a proportional increase with Pt loading, as the protonic pathways are extending with higher thicknesses. This dependency was still observed to a lesser extent for the diluted layers with a constant thickness, indicating possible changes to the ionomer structure caused by the dilution. The pressure independent O_2 diffusion at BoT showed increasing resistances with lower amounts of available Pt down to 0.2 mg_{Pt} cm^{-2} for the un-diluted layers, and constant values for the diluted layers. Looking at the local O_2 diffusion resistance, which was obtained by normalizing to the respective ECSA value, it can be noted that all diluted layers at BoT and EoT, as well as all un-diluted layers above 0.2 mg_{Pt} cm^{-2} at EoT show very similar values, indicating that the local diffusion resistance becomes independent on the Pt loading by either dilution or degradation of the electrode. Only the un-diluted layer with 0.1 mg_{Pt} cm^{-2} showed higher resistances, which might be related to issues in water management in low thickness electrodes.

Acknowledgments

This work was financially supported by the Bundesministerium für Bildung und Forschung (BMBF) under contract No. 03EW0011A (FC-RAT), and the Bundesministerium für Verkehr und digitale Infrastruktur (BMVI) under contract No. 03B11018A (OREO).

The University of Connecticut authors would like acknowledge funding support from NSF PFI-RP award #1919280-Commercializing Active and Durable Materials and Electrodes for Fuel Cell and Electrolyzer Applications. Also, the authors acknowledge Marcia Reid from McMaster University in Canada, for ultramicrotome sample preparation.

Appendix

Table A·I. In-situ parameters and STEM-EDS quantified data for all investigated cathode catalyst layers, at BoT and EoT state, shown in first and second parameter row respectively.

Parameter	Unit	BoT and EoT values						
Pt loading (weighed)	$mg_{Pt}\ cm^{-2}$	0.10	0.20	0.32	0.41	0.09	0.20	0.30
Pt/C ratio	*wt%*	40.0	40.0	40.0	40.0	14.3	25.0	33.3
ECSA	cm^2/cm^2	54.28	95.13	135.95	183.04	46.72	94.91	138.15
		13.53	33.64	58.92	76.93	11.46	32.48	53.34
Prot. CL resistance	$m\Omega\ cm^2$	40.73	70.25	102.54	197.57	103.94	119.93	159.22
		34.80	72.85	113.82	184.37	94.67	117.34	146.65
Double layer capacity	$mF\ cm^{-2}$	21.81	37.01	48.91	75.89	23.55	39.09	56.31
		9.24	21.18	32.09	47.28	18.26	27.29	37.39
Pressure indep. Diffusion resistance	$s\ m^{-1}$	26.10	11.78	9.62	7.62	26.64	12.37	9.10
		101.32	26.41	15.79	11.13	85.08	28.61	18.05
Specific activity @700 mV	$mA\ cm^{-2}{}_{Pt}$	19.15	14.04	11.01	6.91	14.96	11.44	8.87
		13.12	29.83	16.96	11.34	12.57	16.76	14.86
STEM-EDS quant. Pt loading	$mg_{Pt}\ cm^{-2}$	0.1	0.2	0.35	0.4	0.1	0.21	0.33
		0.07	0.14	0.27	0.36	0.09	0.19	0.3
STEM-EDS quant. Pt concentration	$mg_{Pt}\ cm^{-3}$	319.58	300.44	321.78	279.9	64.71	124.53	192.47
		207.15	195.09	294.14	305.3	61.08	126.01	175.5
STEM-EDS quant. Pt concentration (membrane IF)	$mg_{Pt}\ cm^{-3}$	—	—	—	—	—	—	—
		90.16	89.41	84.91	106.86	28.18	46.89	59.11
PSD Mean Particle Size (full CL)	*nm*	2.47 +/− 0.53	1.85 +/− 0.59	2.09 +/− 0.63	1.97 +/− 0.63	2.24 +/− 0.58	2.77 +/− 0.76	3.21 +/− 1.19
		7.97 +/− 3.40	7.54 +/− 3.36	6.92 +/− 2.59	6.77 +/− 1.81	6.30 +/− 2.59	6.87 +/− 3.76	7.05 +/− 2.76
PSD Mean Particle Size (mem. IF)	*nm*	—	—	—	—	—	—	—
		10.05 +/− 3.68	8.20 +/− 3.89	8.47 +/− 3.14	6.98 +/− 2.39	—	—	—
PSD Mean Particle Size (mid)	*nm*	—	—	—	—	—	—	—
		6.59 +/− 2.43	6.33 `/− 2.53	5.59 +/− 1.43	6.39 +/− 1.38	—	—	—
PSD Mean Particle Size (GDL IF)	*nm*	—	—	—	—	—	—	—
		7.36 +/− 2.98	7.95 +/− 3.26	6.76 +/− 2.09	7.11 +/− 1.61	—	—	—

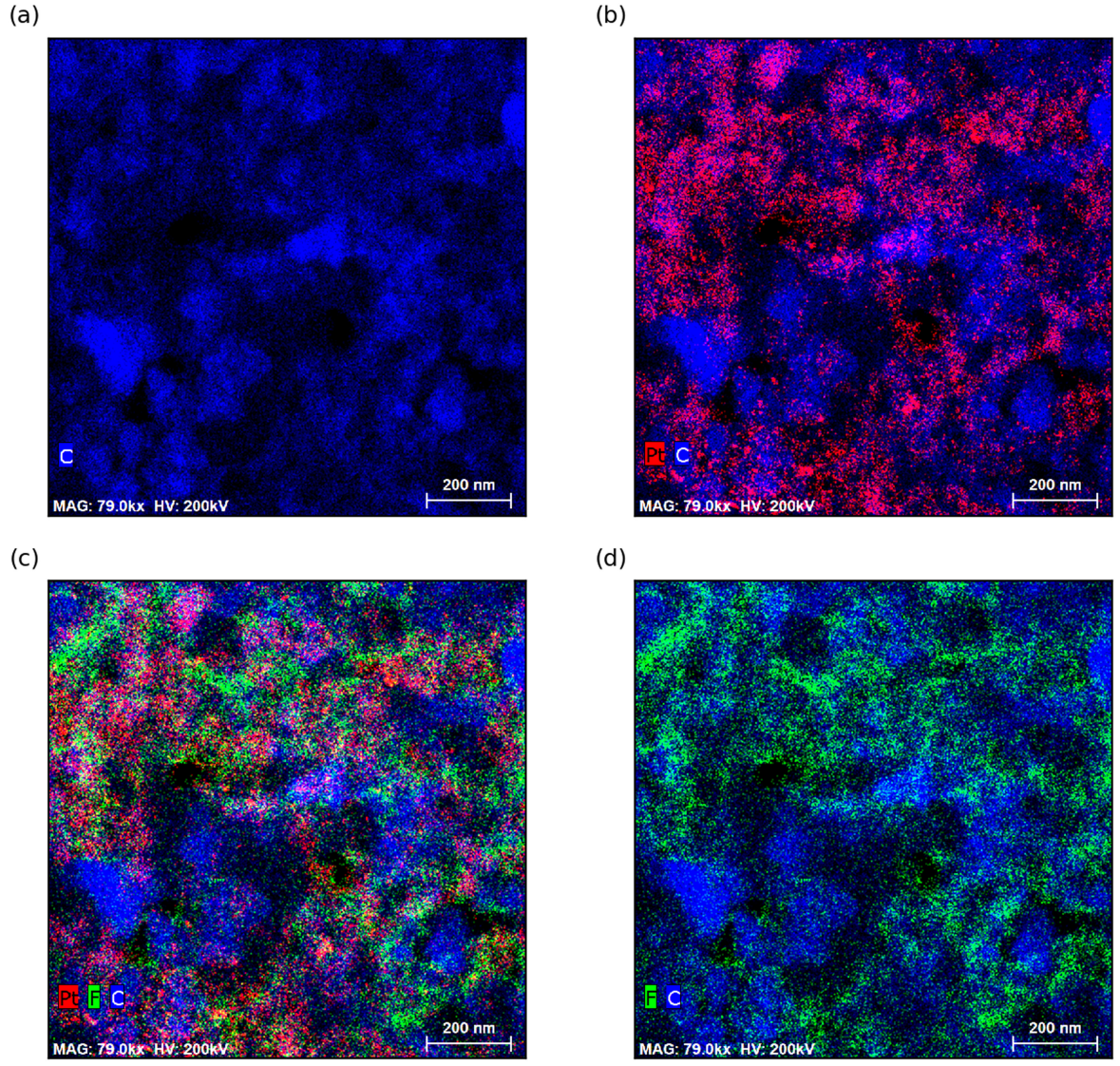

Figure A·I. STEM-EDS maps of a diluted catalyst layer with 0.2 mg_{Pt} cm^{-2} and 25 wt% Pt/C ratio: Distribution of (a) Carbon, (b) Platinum/Carbon, (c) Platinum/Carbon/Fluorine and (d) Fluorine/Carbon.

ORCID

Patrick Schneider https://orcid.org/0000-0002-0796-3489
Mariah Batool https://orcid.org/0000-0001-7692-2915
Dietmar Gerteisen https://orcid.org/0000-0002-6419-3628
Jasna Jankovic https://orcid.org/0000-0001-8267-9560

References

1. N. Zamel, *J. Power Sources*, **309**, 141 (2016).
2. A. Kongkanand and M. F. Mathias, *J. Phys. Chem. Letters*, **7**, 1127 (2016).
3. T. Soboleva, K. Malek, Z. Xie, T. Navessin, and S. Holdcroft, *ACS Appl. Mater. Interfaces*, **3**, 1827 (2011).
4. T. Soboleva, X. Zhao, K. Malek, Z. Xie, T. Navessin, and S. Holdcroft, *ACS Appl. Mater. Interfaces*, **2**, 375 (2010).
5. A.-C. Scherzer, P. Schneider, P. K. Herring, M. Klingele, N. Zamel, and D. Gerteisen, *J. Electrochem. Soc.*, **169** 34509 (2022).
6. R. Alink, R. Singh, P. Schneider, K. Christmann, J. Schall, R. Keding, and N. Zamel, *Molecules*, **25**, 1523 (2020).
7. Y. Garsany, R. W. Atkinson III, M. B. Sassin, and R. Hjelm, *J. Electrochem. Soc.*, **165**, F381 (2018).
8. S. Shahgaldi, I. Alaefour, and X. L. Li, *Appl. Energy*, **225**, 1022 (2018).
9. S. Shahgaldi, I. Alaefour, and X. Li, *Appl. Energy*, **217**, 295 (2018).
10. S. Shahgaldi, A. Ozden, X. Li, and F. Hamdullahpur, *Energy Convers. Manage.*, **171**, 1476 (2018).
11. C.-H. Song and J.-S. Park, *Energies*, **12**, 549 (2019).
12. S. Herden, J. A. Hirschfeld, C. Lohri, M. Perchthaler, and S. Haase, *J. Power Sources*, **364**, 449 (2017).
13. S. Herden, F. Riewald, J. A. Hirschfeld, and M. Perchthaler, *J. Power Sources*, **355**, 36 (2017).
14. J. P. Owejan, J. E. Owejan, and W. Gu, *J. Electrochem. Soc.*, **160**, F824 (2013).
15. F. A. de Bruijn, V. A. T. Dam, and G. J. M. Janssen, *Fuel Cells*, **8**, 3 (2008).
16. Y. Shao-Horn, W. C. Sheng, S. Chen, P. J. Ferreira, E. F. Holby, and D. Morgan, *Top. Catal.*, **46**, 285 (2017).
17. F. N. Büchi, M. Inaba, and T. J. Schmidt, *Proton exchange fuel cell durability* (Berlin)(Springer) (2009).
18. *Cell Component Accelerated Stress Test and Polarization Curve Protocols for PEM Fuel Cells,* https://energy.gov/eere/fuelcells/durability-working-group#accelerated_stress_tests (2013) U.S. DRIVE Fuel Cell Tech Team, .
19. G. S. Harzer, J. N. Schwammlein, A. M. Damjanovic, S. Ghosh, and H. A. Gasteiger, *J. Electrochem. Soc.*, **165**, F3118 (2018).
20. P. Schneider, C. Sadeler, A.-C. Scherzer, N. Zamel, and D. Gerteisen, *J. Electrochem. Soc.*, **166**, F322 (2019).
21. A. Kneer, N. Wagner, C. Sadeler, A.-C. Scherzer, and D. Gerteisen, *J. Electrochem. Soc.*, **165**, F805 (2018).
22. J. D. Fairweather, D. Spernjak, A. Z. Weber, D. Harvey, S. Wessel, D. S. Hussey, D. L. Jacobson, K. Artyushkova, R. Mukundan, and R. L. Borup, *J. Electrochem. Soc.*, **160** (2013).
23. M. Darab, A. O. Barnett, G. Lindbergh, M. S. Thomassen, and S. Sunde, *Electrochim. Acta*, **232**, 505 (2017).
24. F. Hegge, J. Sharman, R. Moroni, S. Thiele, R. Zengerle, M. Breitwieser, and S. Vierrath, *J. Electrochem. Soc.*, **166**, F956 (2019).
25. T. Schuler, A. Chowdhury, A. T. Freiberg, B. Sneed, F. B. Spingler, M. C. Tucker, K. L. More, C. J. Radke, and A. Z. Weber, *J. Electrochem. Soc.*, **166**, F3020 (2019).

26. A. Kneer, J. Jankovic, D. Susac, A. Putz, N. Wagner, M. Sabharwal, and M. Secanell, *J. Electrochem. Soc.*, **165**, F3241 (2018).
27. M. Mayur, M. Gerard, P. Schott, and W. G. Bessler, *Energies*, **11**, 2504 (2018).
28. S. Morando, S. Jemei, D. Hissel, R. Gouriveau, and N. Zerhouni, *Int. J. Hydrogen Energy*, **42**, 1472 (2017).
29. K. More, R. Borup, and K. Reeves, *ECS Trans.*, **3**, 717 (2006).
30. P. Schneider, C. Sadeler, A.-C. Scherzer, N. Zamel, and D. Gerteisen, *J. Electrochem. Soc.*, **166**, F322 (2019).
31. D. Zhou, F. Gao, E. Breaz, A. Ravey, and A. Miraoui, *Energy*, **138**, 1175 (2017).
32. Q. Meyer, I. Pivac, F. Barbir, and C. Zhao, *J. Power Sources*, **470**, 228285 (2020).
33. A. Z. Weber and A. Kusoglu, *J. Mater. Chem. A*, **2**, 17207 (2014).
34. A. Orfanidi, P. Madkikar, H. A. El-Sayed, G. S. Harzer, T. Kratky, and H. A. Gasteiger, *J. Electrochem. Soc.*, **164**, F418 (2017).
35. L. Guetaz, M. Lopez-Haro, S. Escribano, A. Morin, G. Gebel, D. A. Cullen, K. L. More, and R. L. Borup, *ECS Trans.*, **69**, 455 (2015).
36. T. Morawietz, M. Handl, C. Oldani, P. Gazdzicki, J. Hunger, F. Wilhelm, J. Blake, K. A. Friedrich, and R. Hiesgen, *J. Electrochem. Soc.*, **165**, F3139 (2018).
37. R. Makharia, M. F. Mathias, and D. R. Baker, *J. Electrochem. Soc.*, **152**, A970 (2005).
38. D. R. Baker, D. A. Caulk, K. C. Neyerlin, and M. W. Murphy, *J. Electrochem. Soc.*, **156**, B991 (2009).
39. U. Beuscher, *J. Electrochem. Soc.*, **153**, A1788 (2006).
40. R. M. Darling and J. P. Meyers, *J. Electrochem. Soc.*, **150** A1523 (2003).
41. S. A. Berlinger, A. Chowdhury, T. van Cleve, A. He, N. Dagan, K. C. Neyerlin, B. D. McCloskey, C. J. Radke, and A. Z. Weber, *ACS Appl. Mater. Interfaces*, **14**, 36731 (2022).
42. N. Nonoyama, S. Okazaki, A. Z. Weber, Y. Ikogi, and T. Yoshida, *J. Electrochem. Soc.*, **158**, B416 (2011).
43. T. Muzaffar, T. Kadyk, and M. Eikerling, *Sustainable Energy Fuels*, **2**, 1189 (2018).
44. W. Olbrich, T. Kadyk, U. Sauter, and M. Eikerling, *J. Electrochem. Soc.* (2022).
45. S. M. Andersen, *Appl. Catalysis B*, **181**, 146 (2016).
46. S. M. Andersen and L. Grahl-Madsen, *Int. J. Hydrogen Energy*, **41**, 1892 (2016).